POLITECNICO DI TORINO
Repository ISTITUZIONALE

Gaussian specimens for VHCF tests: Analytical prediction of damping effects

Original
Gaussian specimens for VHCF tests: Analytical prediction of damping effects / Tridello, Andrea; Paolino, Davide Salvatore; Chiandussi, Giorgio; Rossetto, Massimo. - In: INTERNATIONAL JOURNAL OF FATIGUE. - ISSN 0142-1123. - STAMPA. - 83:1(2016), pp. 36-41. [10.1016/j.ijfatigue.2015.04.025]

Availability:
This version is available at: 11583/2615060 since: 2022-06-18T08:02:22Z

Publisher:
Elsevier

Published
DOI:10.1016/j.ijfatigue.2015.04.025

Terms of use:

This article is made available under terms and conditions as specified in the corresponding bibliographic description in the repository

Publisher copyright

(Article begins on next page)

12 October 2024

Gaussian specimens for VHCF tests: analytical prediction of damping effects.

Authors:
A. Tridello[a], D.S. Paolino[b], G. Chiandussi[c], M. Rossetto[d]

[a] Department of Mechanical and Aerospace Engineering, Politecnico di Torino, 10129 Turin, Italy, andrea.tridello@polito.it
[b] Department of Mechanical and Aerospace Engineering, Politecnico di Torino, 10129 Turin, Italy, davide.paolino@polito.it
[c] Department of Mechanical and Aerospace Engineering, Politecnico di Torino, 10129 Turin, Italy, giorgio.chiandussi@polito.it
[d] Department of Mechanical and Aerospace Engineering, Politecnico di Torino, 10129 Turin, Italy, massimo.rossetto@polito.it

Corresponding Author:
A. Tridello
E-mail address: andrea.tridello@polito.it
Full postal address:
C.so Duca degli Abruzzi 24,
Department of Mechanical and Aerospace Engineering – Politecnico di Torino,
10129 – Turin,
ITALY
Phone number: +39.011.090.6913
Fax number: +39.011.090.6999

Abstract:

Experimental tests investigating Very-High-Cycle Fatigue (VHCF) properties of materials are commonly performed with ultrasonic testing machines. Ultrasonic tests allow for a significant reduction of testing time but also induce a relevant temperature increment in specimens. Temperature increase can be even dramatic, depending on testing conditions and on specimen shape and material. In particular, due to the large volume of material (risk-volume) under test, Gaussian specimens recently introduced for investigating size effects in VHCF are extremely prone to heat dissipation and to the consequent temperature increment. They were originally designed by the Authors without taking into account the hysteretic damping and its effects both on the stress distribution and on the heat dissipation. However, in order to evaluate the temperature increment and the feasibility of ultrasonic fatigue tests with Gaussian specimens, the total power dissipation and the distribution of the power density dissipated along the specimen must be taken into account.

The present paper proposes an analytical model that permits to evaluate the effects of the hysteretic damping on the stress distribution, on the distribution of the power density and on the total power dissipation in Gaussian specimens. The theoretical model is verified through Finite Element Models and experimentally validated.

Keywords:

Gigacycle fatigue; very-high-cycle fatigue; risk-volume; ultrasonic testing machine; power dissipated.

1. Introduction

In recent years, Very-High-Cycle Fatigue (VHCF) behavior of metallic materials has become a major point of interest for researchers and industries. The needs of specific industrial fields (aerospace, mechanical and energy industry) for structural components with increasingly large fatigue lives, up to 10^{10} cycles (gigacycle fatigue), requested for a more detailed investigation on the experimental properties of materials in the VHCF regime.

Gigacycle fatigue tests are commonly performed using resonance testing machines [1,2] with a loading frequency of 20 kHz (ultrasonic tests). Experimental results on high-strength steels showed that failure is due to cracks which nucleate at the specimen surface (surface nucleation) if the stress amplitude is above the conventional fatigue limit and that failure is generally due to cracks which nucleate from inclusions or internal defects (internal nucleation) when specimens are subjected to stress amplitudes below the conventional fatigue limit [3]. Following the experimental evidence, new phenomenological models for the description of fatigue life were also introduced [4]: models that can take into account the occurrence of two different failure modes (Duplex S-N curves) integrated classical fatigue life models characterized by failures due to a single failure mode and by the presence of the fatigue limit.

Together with the introduction of new fatigue life models, research on VHCF focused also on the study of the effects of different factors on material properties (e.g., stress ratio [5,6], load type [7], environment conditions [8]). Recently, size effects in VHCF gained significant attention and specimens with large risk-volumes (volume of material subjected to a stress amplitude above the 90% of the maximum stress) were investigated. In [9-11], experimental tests were carried out with dog-bone specimens made of high-strength steel. Experimental results in [9-11] showed that fatigue strength significantly decreases if the risk-volume is increased up to 1000 mm^3. Larger risk-volumes were not investigated because the non-uniform stress distribution along the dog-bone specimen part with constant cross section prevented from a further increase of risk-volume.

In [12] the Authors proposed the adoption of Gaussian specimens with risk-volumes larger than 1000 mm^3 for VHCF testing (Figure 1). The design of Gaussian specimens described in [12] was carried out without taking into account the hysteretic damping and its effect on power dissipation. However, hysteretic damping must be considered to assess the feasibility of ultrasonic tests with Gaussian specimens having large risk-volumes.

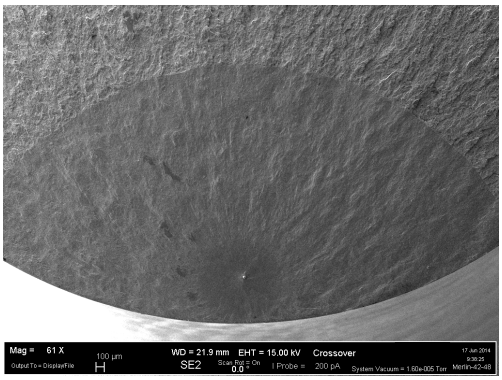

Figure 1: Fracture surface of a Gaussian specimen with 2000 mm^3 risk-volume (N_f=1.5×10^9; σ_a=510 MPa).

The present paper proposes an analytical model for the prediction of the stress distribution and of the power dissipation, in case of Gaussian specimens with hysteretic damping. The Gaussian profile is approximated with a cosine function and the analytical models of the stress distribution, of the distribution of the power density dissipated along the specimen and of the total power dissipation are determined. The analytical models are numerically validated through a Finite Element Analysis by considering Gaussian specimens with risk-volumes ranging from 1000 mm^3 to 5200 mm^3 and are finally experimentally validated by using a Gaussian specimen with a 2000 mm^3 risk-volume.

2. Specimen shape with uniform stress distribution

Internal dissipation in Gaussian specimens is modeled by considering a hysteretic damping model. The complex elastic modulus E_d ($E_d = E_r(1 + \mathbb{i}\,\eta)$) is introduced in order to take into account the hysteretic damping: the real part of the elastic modulus, E_r, takes into account the elastic energy stored by the vibrating body, while the imaginary part ηE_r, being η the loss factor, takes into account the amount of energy dissipated due to internal dissipation. In presence of hysteretic damping, a closed-form solution for the stress distribution in the Gaussian specimen part cannot be determined. Therefore, the Gaussian profile is approximated with a cosine function (Section 2.1), which allows for the computation of the stress distribution along the longitudinal axis of the specimen (Section 2.2). Finally, the power density dissipated along the longitudinal axis and the total power dissipation are analytically determined (Section 2.3).

2.1. Approximation of the Gaussian profile

Figure 1 shows the typical shape of a Gaussian specimen [12].

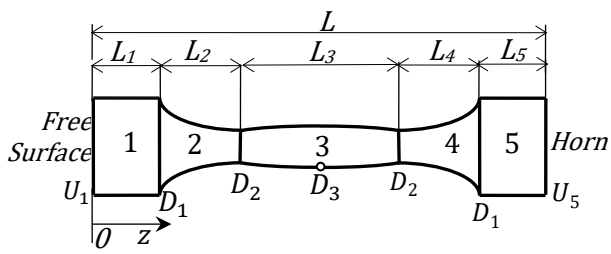

Fig. 2. Typical Gaussian specimen.

In order to determine the displacement and the stress amplitude in specimen part 3, the Gaussian profile is approximated with a cosine function. The approximating cosine function describing the cross-section diameter, $D(z)$, can be obtained by imposing the passage through the points $(L_1 + L_2; D_2)$ and $(L/2 = L_1 + L_2 + L_3/2\,; D_3)$ defined in Fig. 1. The approximating cosine function is given by:

$$D(z) = D_3 \cos\left[\alpha_3 \left(z - \frac{L}{2}\right)\right], \quad (1)$$

where $\alpha_3 = 2\,\mathrm{acos}\left[\frac{D_2}{D_3}\right]/L_3$. The difference between the exact profile and the approximated profile tends to increase as the length L_3 increases: however, in case of L_3 larger than 50 mm, the cosine approximation attains a maximum percent error smaller than 1%.

2.2. Analytical stress distribution

The displacement amplitude in each specimen part ($j = 1, \dots, 5$ in Fig. 1) can be expressed by Equation 2:

$$\begin{cases} u_1[z_1] = (A_{1r} + \mathbb{i}A_{1\mathbb{i}})\cos[kz_1] + (B_{1r} + \mathbb{i}B_{1\mathbb{i}})\sin[kz_1], & 0 \le z_1 \le L_1 \\ u_2[z_2] = \frac{(A_{2r}+\mathbb{i}A_{2\mathbb{i}})\cos + (B_{2r}+\mathbb{i}B_{2\mathbb{i}})\sin}{\cosh[\alpha_2(z_2 - L_2)]}, & 0 \le z_2 \le L_2 \\ u_3[z_3] = \frac{(A_{3r}+\mathbb{i}A_{3\mathbb{i}})\cos + (B_{3r}+\mathbb{i}B_{3\mathbb{i}})\sin}{\cos\left[\alpha_3\left(z_3 - \frac{L_3}{2}\right)\right]}, & 0 \le z_3 \le L_3, \\ u_4[z_4] = \frac{(A_{4r}+\mathbb{i}A_{4\mathbb{i}})\cos + (B_{4r}+\mathbb{i}B_{4\mathbb{i}})\sin}{\cosh[\alpha_2 z_4]}, & 0 \le z_4 \le L_4 \\ u_5[z_5] = (A_{5r} + \mathbb{i}A_{5\mathbb{i}})\cos[kz_5] + (B_{5r} + \mathbb{i}B_{5\mathbb{i}})\sin[kz_5], & 0 \le z_5 \le L_5 \end{cases} \quad (2)$$

where $u_j[\cdot]$ denotes the displacement amplitude in each specimen part ($j = 1 \dots 5$) and A_{jr}, B_{jr}, $A_{j\mathbb{i}}$ and $B_{j\mathbb{i}}$ ($j = 1, \dots, 5$) are the 20 complex coefficients that can be determined by imposing proper boundary conditions: $k = 2 \cdot \pi \cdot f_0 / \sqrt{\frac{E_d}{\rho}}$, being f_0 the resonance frequency and ρ the density, and $\alpha_2 = \mathrm{acosh}[N_2]/L_2$, being N_2 the ratio D_1/D_2.

At the free specimen surface ($z = 0$), the real part of the displacement amplitude is equal to U_1 (Fig. 1), while the imaginary part of displacement amplitude and the real and imaginary parts of the strain amplitude are equal to 0:

$$\begin{cases} \mathrm{Re}[u_1[z_1 = 0]] = U_1 \\ \mathrm{Im}[u_1[z_1 = 0]] = 0 \\ \mathrm{Re}[\varepsilon_1[z_1 = 0]] = 0 \\ \mathrm{Im}[\varepsilon_1[z_1 = 0]] = 0 \end{cases}, \quad (3)$$

where $\varepsilon_j[\cdot]$ denotes the strain amplitude in each specimen part ($j = 1 \dots 5$). The other constant coefficients are determined by imposing the continuity of the real and imaginary parts of the displacement and strain amplitudes at the interface between two adjacent specimen parts:

$$\begin{cases} \mathrm{Re}\left[u_i[z_i = L_i]\right] = \mathrm{Re}\left[u_{i+1}[z_{i+1} = 0]\right] \\ \mathrm{Im}\left[u_i[z_i = L_i]\right] = \mathrm{Im}\left[u_{i+1}[z_{i+1} = 0]\right] \\ \mathrm{Re}\left[\varepsilon_i[z_i = L_i]\right] = \mathrm{Re}\left[\varepsilon_{i+1}[z_{i+1} = 0]\right] \\ \mathrm{Im}\left[\varepsilon_i[z_i = L_i]\right] = \mathrm{Im}\left[\varepsilon_{i+1}[z_{i+1} = 0]\right] \end{cases}, \quad (4)$$

for $i = 1, \dots, 4$ (it is worth noting that, due to symmetry, L_4 is equal to L_2 and L_5 is equal to L_1). The stress distribution in each specimen part is $\sigma_j[z_j] = E_d \varepsilon_j[z_j]$ ($j = 1, \dots, 5$).

2.3. Analytical model for dissipated power

Due to the hysteretic damping, power is dissipated along the Gaussian specimen. Equation 5 expresses the power density dissipated [13] in each specimen part ($j = 1, \dots, 5$):

$$\dot{q}_j[z_j] = \frac{1}{T}\int_0^T \mathrm{Re}\left[\sigma_j[z_j, t]\right] \cdot \mathrm{Re}\left[\frac{\partial \varepsilon_j[z_j, t]}{\partial t}\right] dt, \quad (5)$$

where $\mathrm{Re}\left[\sigma_j[z_j, t]\right]$ is the real part of the stress amplitude in the j-th specimen part, $\mathrm{Re}\left[\frac{\partial \varepsilon_j[z_j, t]}{\partial t}\right]$ is the real part of the I derivative of the strain amplitude with respect to time in the j-th specimen part and T is the load period. By assuming the linear elasticity of the material and by using the exponential notation for complex numbers, Equation 5 can be rewritten as:

$$\bar{\dot{q}} = 2\pi {f_0}^2 \left|\varepsilon_j[z_j]\right|^2 E_r \sqrt{1+\eta^2} \int_0^T \mathrm{Re}\left[e^{\mathbb{i}(2\pi f_0 t + \varphi_j + \arctan[\eta])}\right] \mathrm{Re}\left[\mathbb{i} e^{\mathbb{i}(2\pi f_0 t + \varphi_j)}\right] dt, \quad (6)$$

where $\left|\varepsilon_j[z_j]\right|$ is the Euclidean norm of the strain amplitude in the j-th specimen part (i.e., $\left|\varepsilon_j[z_j]\right| = \sqrt{\mathrm{Re}\left[\varepsilon_j[z_j]\right]^2 + \mathrm{Im}\left[\varepsilon_j[z_j]\right]^2}$) and φ_j is the argument of the complex strain amplitude in the j-th specimen part. With simple passages, Equation 6 can be rewritten as:

$$\bar{\dot{q}} = -2\pi f^2 \left|\varepsilon_j[z_j]\right|^2 E_r \left(\int_0^T \frac{\sin[2(2\pi f_0 t + \varphi_j)]}{2} dt - \int_0^T \eta \sin\left[2\pi f_0 t + \varphi_j\right]^2 dt\right). \quad (7)$$

Finally, by solving the integrals on the right-hand side of Equation 7, the power density dissipated in the j-th specimen part can be expressed as:

$$\dot{q}_j(z_j) = E_r \pi \eta f_0 \left|\varepsilon_j[z_j]\right|^2. \quad (8)$$

The total power dissipation is the dissipated power density (Equation 8) integrated with respect to the volume of each specimen part:

$$\dot{Q} = \sum_{j=1}^{5} \int_0^{L_j} \dot{q}_j[z_j] \cdot S_j[z_j] dz_j, \quad (9)$$

where $S_j[z_j]$ and L_j denote the cross-section and the length of the j-th specimen part, respectively.

It is worth noting that the total power dissipation must be equal to the mechanical power supplied by the ultrasonic generator during one cycle (i.e., $\dot{Q} = \frac{1}{T}\int_0^T S_5[L_5] \cdot \mathrm{Re}\left[\sigma_5[L_5, t]\right] \cdot \mathrm{Re}\left[\frac{\partial \varepsilon_5[L_5, t]}{\partial t}\right] dt$).

3. Finite Element Model verification

The power density dissipated along the specimen length and the total power dissipation at the first longitudinal frequency are evaluated through Finite Element Analyses (FEA) for four Gaussian specimens with increasing risk-volumes. The characteristics of each specimen are reported in Table 1:

	D_2 [mm]	L_3 [mm]	Risk-volume [mm^3]
Specimen 1	8	20	1200
Specimen 2	10	20	1974
Specimen 3	8	55	3124
Specimen 4	10	55	5118

Table 1. Characteristics of specimens used for FEA.

The numerical analyses were carried out by using the commercial finite element program ANSYS. Eight-node quadrilateral elements (plane 82) with the axis-symmetric option are used for the finite element models. The numerical models count for a number of elements ranging from 12000 to 25000 elements. The Gaussian specimens considered for the analysis were designed considering steel (E_r equal to $211\ \mathrm{GPa}$, Poisson's ratio equal to 0.29, material density equal to $7800\ kg/m^3$ and loss factor η equal to 0.00047 [14]). The specimens were loaded by imposing a harmonic nodal displacement at the interface between specimen and horn ($z = L$). The harmonic displacement were determined by considering the analytical amplification factor [12] in order to have a stress amplitude equal to $500\ \mathrm{MPa}$ in the Gaussian specimen part.

For each Gaussian specimen, Figure 3 reports the power density dissipated with respect the non-dimensional coordinate (z/L). The power density dissipated computed by using the longitudinal stress distribution obtained with the analytical model and the power density dissipated computed by using the longitudinal stress distribution along the longitudinal axis obtained with FEA are plotted.

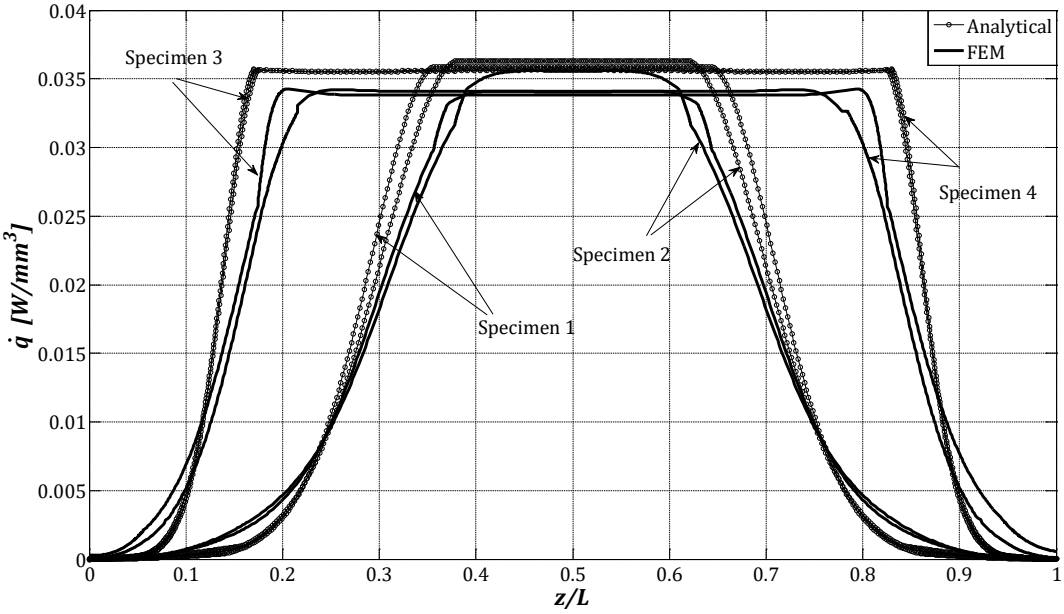

Fig. 3. Power density along the longitudinal axis.

According to Figure 3, the power densities computed by using the analytical model and the numerical model have similar qualitative trends. However, the FEA model gives smaller maximum densities: for the same applied harmonic displacement, the stresses in the Gaussian specimen part computed through FEA is about 1.5% smaller than the stresses computed through the analytical model. As a consequence, the power density computed through FEA is smaller, according to Equation 5. The difference increases as the Gaussian specimen length increases: however, for the analyzed cases, the maximum difference is smaller than $0.002\ W/mm^3$.

Finally, the total power dissipation were evaluated by using the analytical model (Equation 9) and through FEA. Considering FEA, the total power dissipation were evaluated as the sum of the power densities dissipated (Equation 8) in each element multiplied by the volume of the corresponding element. Both normal strains and shear strains are considered for the computation in FEA.

Table 2 reports the total power dissipation evaluated by considering the analytical model and FEA together with the percent difference.

	Analytical model [W]	*FEA model [W]*	*Percent difference*
Specimen 1	65	72	10%
Specimen 2	105	119	11%
Specimen 3	131	144	9%
Specimen 4	211	238	11%

Table 2. Total power dissipation obtained through the analytical model and through FEA.

According to Table 2, the total power dissipation is larger if computed through FEA. In the computation of the total power dissipation with FEA, the contribution of each stress component is taken into account, while, in the analytical model, only the longitudinal normal stress is considered for the power computation. For the considered cases, the percent difference between the results obtained by using the two approaches is limited and ranges from 9% to 11%. The Gaussian specimen with the largest risk-volume shows the largest total power dissipation: however, it must be noted that the largest total power dissipation is significantly smaller than the maximum mechanical power which can be supplied by ultrasonic generators commonly used for VHCF tests (between $2\ \mathrm{kW}$ and $4\ \mathrm{kW}$).

In general, the difference between the analytical and the numerical models, both for limited risk-volumes and for larger risk-volumes, can be reduced to less than 2% by increasing systematically the total power dissipation computed with the analytical model by about 10%.

6. Experimental validation

The analytical model for the estimation of the total power dissipation were finally validated through an experimental test. A Gaussian specimen with a risk-volume equal to $2000\ \mathrm{mm}^3$ made of an AISI H13 tool steel were used for the experimental validation. The AISI H13 characteristics (E_r and η) were determined through the Impulse Excitation Technique (IET) by using a rectangular bar with the dimensions prescribed in [16]. The rectangular bar, supported at the node for the longitudinal mode of vibration was hit at one of the antinodes by using a small hammer. At the other antinode the vibration amplitude was acquired by using a microphone and used for the determination of E_r and η. E_r, equal to $211.8\ \mathrm{GPa}$, was computed according to [16]. The loss factor η, equal to 0.000127, was determined by considering the logarithmic decrement method.

The experimental validation of the analytical model for the estimation of the total power dissipation was carried out by using an ultrasonic testing machine developed at the Politecnico di Torino [15]. The specimen was loaded at a stress amplitude equal to $500\ \mathrm{MPa}$; the stress amplitude in the Gaussian specimen part was kept constant through a closed-loop controller based on the displacement measured at the free specimen surface. A strain gage calibration was also performed before the test. The specimen was loaded for 5 seconds.

The total power dissipation in the Gaussian specimen ($\dot{Q}_{exp}$) was evaluated as reported in Equation 10:

$$\dot{Q}_{exp} = \dot{Q}_{tot} - \dot{Q}_0, \quad (10)$$

where $\dot{Q}_{tot}$ is the mean value (averaged over the acquisition time) of the total power dissipation when the test was run with the specimen, while $\dot{Q}_0$ is the mean value (averaged over the acquisition time) of the total power dissipation when the test was run without the specimen. $\dot{Q}_{tot}$ and $\dot{Q}_0$ were acquired from the ultrasonic generator (Branson Ultrasonics DCX S 20:4.0) at a sample rate of $300\ \mathrm{kHz}$ with a data acquisition card NI PCIe-6363.

The measured total power dissipation is equal to $42\ \mathrm{W}$. In good agreement with the experimental result, a value of $41\ \mathrm{W}$ is obtained if the total power dissipation is computed analytically and is increased by 10%, according to the correction proposed in Section 3.

5. Conclusions

An analytical model for the evaluation of the stress distribution, of the power density distribution and of the total power dissipation in Gaussian specimens was proposed in the paper. The analytical model was verified through FEA. Considering the total power dissipation, the difference between the two approaches was in general limited (about 10%) and could be reduced to less than 2% with a systematic correction of the analytical prediction. Moreover, in the investigated cases the total power dissipation ($215\ \mathrm{W}$ for the largest risk-volume) was found to be significantly smaller than the maximum mechanical power that can be supplied by ultrasonic generators commonly adopted for VHCF tests.

Finally, the analytical model was experimentally validated with a Gaussian specimen having a risk-volume equal to 2000 mm^3: the measured total power dissipation was in good agreement with the analytical prediction (percent error smaller than 5%).

A1. Appendix 1: Coefficients involved in Equation 2

For the determination of the stress distribution along the Gaussian specimen, the 20 unknown constant coefficients A_{jr}, B_{jr} and $A_{j\mathbb{i}}$, $B_{j\mathbb{i}}$ ($j = 1, \dots, 5$) in Equation 2 must be determined.

By considering specimen part 1, the constant coefficients A_{1r}, $A_{1\mathbb{i}}$, B_{1r} and $B_{1\mathbb{i}}$ are easily obtained by considering that the displacement amplitude must be maximum and equal to U_1:

$$\begin{Bmatrix} A_{1r} \\ A_{1\mathbb{i}} \\ B_{1r} \\ B_{1\mathbb{i}} \end{Bmatrix} = \begin{Bmatrix} U_1 \\ 0 \\ 0 \\ 0 \end{Bmatrix}. \qquad \text{(A1)}$$

The other constant coefficients are determined by imposing the continuity of the real and imaginary part of displacement amplitude and strain amplitude at the interface between two adjacent specimen parts. By solving Equation 4, the unknown coefficients in the i-th specimen part ($i = 2, \dots, 5$) can be expressed as a function of the coefficients obtained for the $(i-1)$-th specimen part (Equation A2):

$$\begin{Bmatrix} A_{ir} \\ A_{i\mathbb{i}} \\ B_{ir} \\ B_{i\mathbb{i}} \end{Bmatrix} = \boldsymbol{T_i} \begin{Bmatrix} A_{(i-1)r} \\ A_{(i-1)\mathbb{i}} \\ B_{(i-1)r} \\ B_{(i-1)\mathbb{i}} \end{Bmatrix}, \qquad \text{(A2)}$$

where $\boldsymbol{T_i}$ is the matrix that allows to determine the unknown coefficients of the i-th specimen part from the constant coefficients of the $(i-1)$-th specimen part.

In order to simplify the computation, geometrical parameters must be at first defined: let $\beta_{3r} = \mathrm{Re}[\beta_3]$, $\beta_{3\mathbb{i}} = \mathrm{Im}[\beta_3]$, $\beta_{2r} = \mathrm{Re}[\beta_2]$, $\beta_{2\mathbb{i}} = \mathrm{Im}[\beta_2]$, $k_r = \mathrm{Re}[k]$, $k_{\mathbb{i}} = \mathrm{Im}[k]$, $L_{1r} = L_1 k_r$, $L_{1\mathbb{i}} = L_1 k_{\mathbb{i}}$,$L_{2r} = L_2 \beta_{2r}$, $L_{2\mathbb{i}} = L_2 \beta_{2\mathbb{i}}$, $L_{3r} = L_3 \beta_{3r}$, $L_{3\mathbb{i}} = L_3 \beta_{3\mathbb{i}}$, $\theta_2 = \beta_{2r}/\beta_{2\mathbb{i}}$, $\theta_3 = \beta_{3r}/\beta_{3\mathbb{i}}$, $\theta_k = k_r/k_{\mathbb{i}}$, $K_{2k} = (1 + \theta_k \theta_2)$, $K_k = (\theta_2 - \theta_k)$, $K_{23} = (\theta_2 - \theta_3)$ and $K_3 = (1 + \theta_3 \theta_2)$.

Matrix $\boldsymbol{T_i}$ for each specimen part ($\boldsymbol{T_i^T}$ is the transpose of the matrix $\boldsymbol{T_i}$) is reported from Equation A3 to Equation A6.

- Specimen part 2:

$$E_1 \begin{bmatrix} N_2 \cos[L_{1r}] \cosh[L_{1\mathbb{i}}]/E_1 & 0 & 0 & 0 \\ -N_2 \sin[L_{1r}] \sinh[L_{1\mathbb{i}}]/E_1 & 0 & 0 & 0 \\ \left(-K_{2k} \tan[L_{1r}] + K_k \tanh[L_{1\mathbb{i}}] + \frac{\alpha_2 (\tan[L_{1r}] \tanh[L_{1\mathbb{i}}] - \theta_2)}{k_{\mathbb{i}} \coth[L_2 \alpha_2]}\right) & 0 & 0 & 0 \\ \left(-K_k \tan[L_{1r}] - K_{2k} \tanh[L_{1\mathbb{i}}] + \frac{\alpha_2 (1 + \tan[L_{1r}] \tanh[L_{1\mathbb{i}}] \theta_2)}{k_{\mathbb{i}} \coth[L_2 \alpha_2]}\right) & 0 & 0 & 0 \end{bmatrix}, \qquad \text{(A3)}$$

where $E_1 = \frac{N_2 k_{\mathbb{i}} \beta_{2\mathbb{i}} \cos[L_{1r}]}{\beta_{2m}^2 \mathrm{sech}[L_{1\mathbb{i}}]}$, being $\beta_{2m} = |\beta_2|$.

- Specimen part 3:

$$F_1\begin{bmatrix} \frac{N_3\cos[L_{2r}]}{F_1\mathrm{sech}[L_{2i}]} & \frac{N_3\sin[L_{2r}]}{F_1\mathrm{csch}[L_{2i}]} & F_2\theta_3 - K_3F_3 - \frac{(K_{23}+F_2F_3)}{\coth[L_{2i}]} & -F_2 + K_{23}F_3 - \frac{(K_3+F_2\theta_3F_3)}{\coth[L_{2i}]} \\ \frac{N_3\sin[L_{2r}]}{F_1\mathrm{csch}[L_{2i}]} & \frac{-N_3\cos[L_{2r}]}{F_1\mathrm{sech}[L_{2i}]} & F_2 - K_{23}F_3 + \frac{(K_3+F_2\theta_3F_3)}{\coth[L_{2i}]} & F_2\theta_3 - K_3F_3 - \frac{(K_{23}+F_2F_3)}{\coth[L_{2i}]} \\ \frac{N_3\sin[L_{2,r}]}{F_1\mathrm{sech}[L_{2i}]} & \frac{-N_3\cos[L_{2r}]}{F_1\mathrm{csch}[L_{2i}]} & K_3 + F_2\theta_3F_3 + \frac{(F_2-K_{23}F_3)}{\coth[L_{2i}]} & -K_{23} - F_2F_3 + \frac{(F_2\theta_3-K_3F_3)}{\coth[L_{2i}]} \\ \frac{-N_3\cos[\mathrm{L}_{2r}]]}{F_1\mathrm{csch}[L_{2i}]} & \frac{-N_3\sin[L_{2r}]}{F_1\mathrm{sech}[L_{2i}]} & K_{23} + F_2F_3 - \frac{(F_2\theta_3-K_3F_3)}{\coth[L_{2i}]} & K_3 + F_2\theta_3F_3 + \frac{(F_2-K_{23}F_3)}{\coth[L_{2i}]} \end{bmatrix}^T, \quad \text{(A4)}$$

where $F_1 = \frac{N_3\beta_{2i}\beta_{3i}\cos[L_{2r}]}{\mathrm{sech}[L_{2i}]\beta_{3m}^2}$, being $\beta_{3m} = |\beta_3|$, $F_2 = \frac{\alpha_3}{\beta_{2i}\cot[L_3\alpha_3]}$, $F_3 = \tan[L_{2r}]$.

- Specimen part 4:

$$G_1\begin{bmatrix} \frac{\cos[2L_{3r}]}{G_1N_3\mathrm{Sech}[2\mathrm{L}_{3i}]} & \frac{-\sin[2\mathrm{L}_{3r}]}{G_1N_3\mathrm{csch}[2\mathrm{L}_{3i}]} & K_3 - G_2G_3\theta_2 + \frac{(\mathrm{G}_2-\mathrm{G}_3K_{23})}{\coth[2L_{3i}]} & G_2G_3 + K_{23} + \frac{(\mathrm{G}_3K_3+\mathrm{G}_2\theta_2)}{\coth[2L_{3i}]} \\ \frac{\sin[2L_{3r}]}{G_1N_3\mathrm{csch}[2\mathrm{L}_{3i}]} & \frac{\cos[2\mathrm{L}_{3r}]}{G_1N_3\ \mathrm{sech}[2\mathrm{L}_{3i}]} & -G_2G_3 - K_{23} - \frac{(\mathrm{G}_3K_3+\mathrm{G}_2\theta_2)}{\coth[2L_{3i}]} & K_3 - G_2G_3\theta_2 + \frac{(\mathrm{G}_2-\mathrm{G}_3K_{23})}{\coth[2L_{3i}]} \\ \frac{\sin[2L_{3r}]}{G_1N_3\mathrm{sec}[2\mathrm{L}_{3i}]} & \frac{\cos[2\mathrm{L}_{3r}]}{G_1N_3\mathrm{csch}[2\mathrm{L}_{3i}]} & -G_3K_3 - G_2\theta_2 - \frac{(\mathrm{G}_2\mathrm{G}_3+K_{23})}{\coth[2L_{3i}]} & G_2 - \mathrm{G}_3K_{23} + \frac{(K_3-\mathrm{G}_2\mathrm{G}_3\theta_2)}{\coth[2L_{3i}]} \\ \frac{-\cos[2L_{3r}]}{G_1N_3\mathrm{csch}[2\mathrm{L}_{3i}]} & \frac{\sin[2\mathrm{L}_{3r}]}{G_1N_3\ \mathrm{sech}[2\mathrm{L}_{3r}]} & -G_2 + G_3K_{23} - \frac{(\mathrm{K3}-\mathrm{G}_2\mathrm{G}_3\theta_2)}{\coth[2L_{3i}]} & -\mathrm{G}_3K_3 - G_2\theta_2 - \frac{(\mathrm{G}_2\mathrm{G}_3+K_{23})}{\coth[2L_{3i}]} \end{bmatrix}^T, \quad \text{(A5)}$$

where $G_1 = -\frac{\beta_{2i}\beta_{3i}\cosh[2L_{3i}]}{N_3\csc[2L_{3r}]\beta_{2m}^2}$, $G_2 = \frac{\alpha_3\sin[L_3\alpha_3]}{N_3\beta_{3i}}$ and $G_3 = \cot[2L_{3r}]$.

- Specimen part 5:

$$I_1\begin{bmatrix} \frac{\cos[L_{2r}]}{I_1N_2\mathrm{sech}[L_{2i}]} & \frac{-\sin[L_{2r}]}{I_1N_2\mathrm{csch}[L_{2i}]} & \frac{K_{2k}}{{I_4}^{-1}} + \frac{I_2I_3\theta_k-I_2\mathrm{I}_5}{\cosh[L_{2i}]} + \frac{I_3I_4K_k}{\coth[L_{2i}]} & \frac{-K_k}{{I_4}^{-1}} + \frac{I_3I_4K_{2k}}{\coth[L_{2i}]} - \frac{I_2(I_3+\theta_kI_5)}{\cosh[L_{2i}]} \\ \frac{\sin[L_{2r}]}{I_1N_2\mathrm{csch}[L_{2i}]} & \frac{\cos[L_{2r}]}{I_1N_2\ \mathrm{sech}[L_{2i}]} & \frac{K_k}{{I_4}^{-1}} + \frac{I_2(I_3+\theta_k\mathrm{I}_5)}{\cosh[L_{2i}]} - \frac{I_3I_4K_{2k}}{\coth[L_{2i}]} & \frac{K_{2k}}{{I_4}^{-1}} + \frac{I_2I_3\theta_k-I_2\mathrm{I}_5}{\mathrm{Cosh}[L_{2i}]} + \frac{I_3I_4K_k}{\mathrm{Coth}[L_{2i}]} \\ \frac{\sin[L_{2r}]}{I_1N_2\mathrm{sech}[L_{2i}]} & \frac{\cos[L_{2r}]}{I_1N_2\mathrm{csch}[L_{2i}]} & \frac{-I_3K_{2k}}{{I_4}^{-1}} + \frac{I_2(\theta_k+I_3\mathrm{I}_5)}{\cosh[L_{2i}]} + \frac{I_4K_k}{\coth[L_{2i}]} & \frac{I_3K_k}{{I_4}^{-1}} + \frac{I_4K_{2k}}{\mathrm{Coth}[L_{2i}]} - \frac{I_2(1-I_3\theta_kI_5)}{\mathrm{Cosh}[L_{2i}]} \\ \frac{-\cos[L_{2r}]}{I_1N_2\mathrm{csch}[L_{2i}]} & \frac{\sin[L_{2r}]}{I_1N_2\ \mathrm{sech}[L_{2i}]} & \frac{-I_3K_k}{{I_4}^{-1}} + \frac{I_2(1-I_3\theta_k\mathrm{I}_5)}{\cosh[L_{2i}]} - \frac{I_4K_{2k}}{\coth[L_{2i}]} & \frac{-I_3K_{2k}}{{I_4}^{-1}} + \frac{I_4K_k}{\mathrm{Coth}[L_{2i}]} + \frac{I_2(\theta_k+I_3I_5)}{\mathrm{Cosh}[L_{2i}]} \end{bmatrix}^T, \quad \text{(A6)}$$

where $I_1 = -\frac{k_i\sin[L_{2r}]\cosh[L_{2i}]}{{k_m}^2 4{N_2}^3}$, $I_2 = \frac{2\alpha_2\sinh[2\alpha_2L_2]}{\mathrm{sech}[L_{2i}]}$, $I_3 = \cot[L_{2r}]$, $I_4 = 4{N_2}^2\beta_{2i}$ and $I_5 = \tanh[L_{2i}]$.

References

[1] Bathias C, Paris PC. Gigacycle fatigue in mechanical practice, 2nd ed. New York: CRC Dekker; 2005.

[2] Stanzl-Tschegg S. Very high cycle fatigue measuring techniques, Int J Fatigue 2014; 60: 2-17.

[3] Mughrabi H. On 'multi-stage' fatigue life diagrams and the relevant life-controlling mechanisms in ultrahigh-cycle fatigue. Fatigue Fract Eng Mater Struct 2002; 25: 755-764.

[4] Paolino DS, Chiandussi G, Rossetto M. A unified statistical model for S-N fatigue curves: probabilistic definition. Fatigue Fract Eng Mater Struct 2013; 36: 187-201.

[5] Shiozawa K, Hasegawa T, Kashiwagi Y, Lu L. Very high cycle fatigue properties of bearing steel under axial loading condition. Int J Fatigue 2009; 31: 880–888.

[6] Sakai T Sato Y, Nagano Y, Takeda M, Oguma N. Effect of stress ratio on long life fatigue behavior of high carbon chromium bearing steel under axial loading. Int J Fatigue 2006; 28: 1547–1554.

[7] Akiniwa Y, Stanzl-Tschegg S, Mayer H, Wakita M, Tanaka K. Fatigue strength of spring steel under axial and torsional loading in the very high cycle regime. Int J Fatigue 2008; 30: 2057–2063.

[8] Tokaji K, Ko HN, Nakajima M, Itoga H. Effects of humidity on crack initiation mechanism and associated S-N characteristics in very high strength steels. Mater Sci Eng 2003*; A* 345: 197–206.

[9] Furuya Y, Specimen size effects on gigacycle fatigue properties of high-strength steel under ultrasonic fatigue testing. Scripta Materialia 2008; 58: 1014–1017.

[10] Furuya Y, Size effects in gigacycle fatigue of high-strength steel under ultrasonic fatigue testing. Procedia Engineering 20102; 2: 485–490.

[11] Furuya Y, Notable size effects on very high cycle fatigue properties of high strength steel. Mater Sci Eng 2011; A 528: 5234–5240.

[12] Paolino DS, Tridello A, Chiandussi G, Rossetto M, On specimen design for size effect evaluation in ultrasonic gigacycle fatigue testing. Fatigue Fract Eng Mater Struct 2014; 5: 570-579.

[13] Nashif AD, Jones DIG, Henderson JP, Vibration damping, 1st ed New York: Wiley 1985.

[14] Ashby MF, Materials selection in mechanical design, 4th ed Oxford: Butterwoth-Heinemann, 2010.

[15] Paolino DS, Rossetto M, Chiandussi G, Tridello A. Sviluppo di una macchina a ultrasuoni per prove di fatica gigaciclica. Proceedings of the 41th AIAS Conference, Vicenza 2012 (In Italian).

[16] ASTM Standard E1876-09 (2009), Standard Test Method for Dynamic Young's Modulus, Shear Modulus, and Poisson's Ratio by Impulse Excitation of Vibration, ASTM International, West Conshohocken, PA, 2009.